

1 **Dependency of Particle Size Distribution at Dust Emission on** 2 **Friction Velocity and Atmospheric Boundary-Layer Stability**

3 Yaping Shao¹, Jie Zhang², Masahide Ishizuka³, Masao Mikami⁴, John Leys^{5,6}, Ning Huang²

4 ¹Institute for Geophysics and Meteorology, University of Cologne, Germany

5 ²Key Laboratory of Mechanics on Disaster and Environment in Western China, Lanzhou University, China

6 ³Faculty of Engineering and Design, Kagawa University, Japan

7 ⁴Office of Climate and Environmental Research Promotion, Japan Meteorological Business Support Center, Japan

8 ⁵Department of Planning, Industry and Environment, New South Wales, Australia

9 ⁶The Fenner School of Environment & Society, The Australian National University, Australia

10

11 *Correspondence to:* Jie Zhang (zhang-j@lzu.edu.cn) and Ning Huang (huangn@lzu.edu.cn)

12 **Abstract.** Particle size distribution of dust at emission (dust PSD) is an essential quantity to estimate in dust studies. It has
13 been recognized in earlier research that dust PSD is dependent on soil properties (e.g. whether soil is sand or clay) and
14 friction velocity, u_* , a surrogate for surface shear stress and descriptor for saltation bombardment intensity. This recognition
15 has been challenged in some recent papers, causing a debate on whether dust PSD is “invariant” and the search for its
16 justification. In this paper, we analyse the dust PSD measured in the Japan-Australian Dust Experiment and show that dust
17 PSD is dependent on u_* and on atmospheric boundary-layer (ABL) stability. By simple theoretical and numerical analysis,
18 we explain the two reasons for the latter dependency, both related to enhanced saltation bombardment in convective
19 turbulent flows. First, u_* is stochastic and its probability distribution profoundly influences the magnitude of the mean
20 saltation flux due to the non-linear relationship between saltation flux and u_* . Second, in unstable conditions, turbulence is
21 usually stronger, which leads to higher saltation-bombardment intensity. This study confirms that dust PSD depends on u_* ,
22 and more precisely, on the probability distribution of u_* , which in turn is dependent on ABL stability, and consequently dust
23 PSD is also dependent on ABL. We also show that the dependency of dust PSD on u_* and ABL stability is made complicated
24 by soil surface conditions. In general, our analysis reinforces the basic conceptual understanding that dust PSD depends on
25 saltation bombardment and inter-particle cohesion.

26

27 1 Introduction

28 Gillette (1981) explained that dust emission can be produced by aerodynamic lift and saltation bombardment, but under
29 realistic wind, aerodynamic-lift emission is much weaker than saltation-bombardment emission. This hypothesis was
30 confirmed by Shao et al. (1993). It is recognized that saltation bombardment is the most important mechanism for dust
31 emission, and dust emission rate, F , is proportional to streamwise saltation flux, Q ¹.

32 Rice et al. (1995, 1996) visualized the process of saltation bombardment using wind-tunnel photos: a saltation particle at
33 impact on surface ejects a tiny amount of soil into air, leaving behind a crater. Models for estimating crater size have been
34 developed by, e.g., Lu and Shao (1999). The fraction of dust that gets emitted from the ejection is difficult to estimate,
35 because it depends both on inter-particle cohesion and bombardment intensity. Since inter-particle cohesion depends on
36 particle size, d , the fraction of dust emitted must also depend on d . Thus, for a given soil, the particle size distribution of dust
37 at emission (emission-dust PSD), $p_s(d)$, must depend on saltation bombardment or on friction velocity, u_* ($\sqrt{\tau}/\rho$ with τ being
38 surface shear stress and ρ air density; see Section 4.2 for discussion). Alfaro et al. (1997) confirmed that $p_s(d)$ depends on u_* :
39 as u_* increases, $p_s(d)$ shows a higher fraction of dust of smaller d . Based on this result and the observation that different
40 laboratory techniques for PSD analysis yield profoundly different outcomes, depending on the disturbances applied to the
41 samples (Figure 1), Shao (2001) suggested to use a minimally-disturbed PSD, $p_m(d)$, as the limit of $p_s(d)$ for weak saltation,
42 and a fully-disturbed PSD, $p_f(d)$, as the limit of $p_s(d)$ for strong saltation. In this way, $p_s(d)$ is expressed as a weighted
43 average of $p_m(d)$ and $p_f(d)$

$$44 \quad p_s(d) = \gamma p_m(d) + (1 - \gamma) p_f(d), \quad (1)$$

45 where $0 \leq \gamma \leq 1$ is an empirical function of $u_{*c}(d)$, the threshold friction velocity for particles of size d .

46 What is emission-dust PSD? We distinguish three closely related yet subtly different dust PSDs, namely, emission-dust
47 PSD, airborne-dust PSD, and emission-flux PSD. PSD of dust suspended in air (airborne-dust PSD) has been collected from
48 different places under different conditions. Emission-dust PSD and airborne-dust PSD are identical, if the latter is measured
49 at dust source at height zero. Airborne-dust PSD can be used to approximate emission-dust PSD if it is measured close to the
50 source and the dependency of particle motion in air on particle size can be neglected. For modelling size-resolved dust
51 concentration in air (i.e. solving the dust concentration equation for different particle sizes), emission-dust PSD offers the
52 Dirichlet-type boundary condition. If size-resolved dust-emission-fluxes can be calculated, then we can specify the
53 Neumann-type boundary condition for solving the dust concentration equation. From size-resolved dust-emission-fluxes, an
54 emission-flux PSD can be calculated (Section 2; Section 4.2). Emission-flux PSD is neither emission-dust nor airborne-dust
55 PSD, but describes how vertical dust-concentration gradient depends on particle size. In some earlier publications,
56 unfortunately, the differences between the three dust PSDs are not clearly explained.

¹The ratio $\gamma_b = F/Q$ is a main issue in dust emission studies (Zender et al., 2003; Laurent et al., 2006). Marticorena et al. (1997) showed that γ_b depends on soil clay content. Shao (2004) suggested that γ_b depends on friction velocity, soil type and soil particle size distribution.

57 To our knowledge, emission-dust PSD has never been directly measured, but approximated using airborne-dust PSD
 58 measured at some, often different, heights (e.g. Kok, 2011b, Table S1). Available data of airborne-dust PSDs give the
 59 impression that they do not differ much. It has thus been suggested that airborne-dust PSDs may be “not-so-different” and
 60 hence emission-dust PSDs may also be “not-so-different”. Reid et al. (2008) stated that “on regional scales, common mode
 61 dust is not functionally impacted by production wind speed, but rather influenced by soil properties such as
 62 geomorphology ...”. Kok (2011a, 2011b) proposed a dust emission model by treating dust emission as a process of
 63 aggregate fragmentation by saltation bombardment. Since aggregate fragmentation is similar to brittle fragmentation, the size
 64 distribution produced in the process is scale-invariant (Astrom, 2006). Kok (2011a, 2011b) then proposed an emission-dust
 65 PSD and estimated its parameters from the data listed in Table S1 of Kok (2011b). The proposed emission-dust PSD is
 66 frequently used in dust models (Giorgi et al., 2012; Albani et al., 2014; Pisso et al., 2019). However, whether the “not-so-
 67 different” airborne-dust PSDs justify “brittle fragmentation” as the underlying process for dust emission requires scrutiny.

68 Studies on dust PSD are yet to deliver definitive answers. The airborne-dust PSD measurements of Rosenberg et al. (2014)
 69 pointed to larger fraction of fine particles than in earlier published data. Ishizuka et al. (2008) found that airborne-dust PSD
 70 measured close to surface depends on u_* for a weakly crusted soil. Sow et al. (2009) examined the dependency of emission-
 71 flux PSD on u_* for three dust events and reported that the PSD appeared to be independent on u_* , but differed significantly
 72 between weak and strong events. In line with Sow et al. (2009), Khalfallah et al. (2020) reported that emission-flux PSD
 73 depends on atmospheric boundary-layer (ABL) stability, and attributed this to the dependency of particle diffusivity on
 74 particle size. They stated that the dependency of emission-dust PSD on u_* , as observed by Alfaro et al. (1997), may be of
 75 secondary importance in natural conditions compared to its dependency on ABL stability.

76 The argument of Khalfallah et al. (2020) rests on the preferential particle diffusion in turbulent flows. Csanady (1963)
 77 suggested that particle eddy diffusivity, K_p , is related to eddy diffusivity, K , by

$$78 \quad K_p = K(1 + \beta^2 w_t^2 / \sigma^2)^{-1/2}, \quad (2)$$

79 where β is a coefficient, w_t particle terminal velocity and σ the standard deviation of (vertical) turbulent velocity. The
 80 analyses of Walklate (1987) and Wang and Stock (1993), among many others, reached similar conclusions. For dust particles
 81 smaller than $10\mu\text{m}$, K_p/K is close to one for $\sigma = 0.5 \text{ ms}^{-1}$, and still larger than 0.95 for $\sigma = 0.1 \text{ ms}^{-1}$ (Shao, 2008; Fig. 8.12).
 82 Thus, preferential particle diffusion does not seem to fully explain the dependency of dust PSD on ABL stability.

83 The confusion ground emission-dust PSD prompted us to re-examine the data of Ishizuka et al. (2008) from the Japan-
 84 Australian Dust Experiment (JADE). In JADE, airborne-dust PSD were measured at small height directly above the dust
 85 source and can be assumed to well approximate the emission-dust PSD. By composite analysis for different u_* and ABL
 86 stabilities, we show that dust PSD depends on u_* , supporting the findings of Alfaro et al. (1997), and depends on ABL
 87 stability, consistent with the findings of Khalfallah et al. (2020). But in contrast to Khalfallah et al. (2020), we argue that
 88 these dependencies are not mutually exclusive, but collectively point to the simple physics that emission-dust PSD is
 89 dependent on saltation-bombardment intensity and efficiency.

90 2 JADE Data

91 JADE was carried out during 23 Feb ~ 14 Mar 2006 on an Australian farm at (33°50'42.4"S, 142°44'9.0"E) (Ishizuka et al.,
92 2008, 2014). The 4 km² farmland was flat and homogeneous such that the JADE data are not affected by fetch. In JADE,
93 atmospheric variables, land surface properties, soil PSD, size-resolved sand fluxes and dust concentrations were measured.
94 Size-resolved dust-emission fluxes were estimated from the dust concentration measurements. Three Sand Particle Counters
95 (SPCs) (Mikami et al., 2005) were used to measure the sand fluxes in the size range of 39 - 654 μm in 32 bins at 0.05, 0.1
96 and 0.3 m above ground at a sampling rate of 1 Hz. Using the sand fluxes, q_j ($j = 1, 32$), the PSD of saltation particles
97 (saltation-flux PSD) is estimated for a particle size bin at d_j with bin size Δd_j as

$$98 \quad p(d_j)\Delta d_j = q_j / \sum_{j=1}^{j=32} q_j \quad (2)$$

99 Dust concentration was measured using Optical Particle Counters (OPC) for 8 size groups: 0.3 – 0.6, 0.6 – 0.9, 0.9 – 1.4,
100 1.4 – 2.0, 2.0 – 3.5, 3.5 – 5.9, 5.9 – 8.4 and 8.4 – 12.0 μm at 1, 2 and 3.5 m above ground. The upper size limit for the last
101 bin is not well defined, but set empirically to 12.0 μm such that this bin can still be included in the analysis. Airborne-dust
102 PSD is estimated as

$$103 \quad p(d_j)\Delta d_j = c_j / \sum c_j, \quad (3)$$

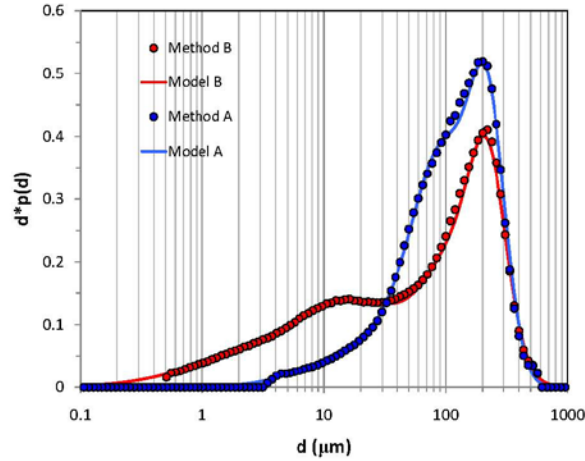
104 where c_j denotes the dust concentration for size bin j . Similarly, the emission-flux PSD can be defined as

$$105 \quad p(d_j)\Delta d_j = F_j / \sum F_j, \quad (3a)$$

106 where F_j denotes the dust flux for size bin j . It should be noted that the emission-flux PSD describes how the covariance of
107 particle-velocity and particle-concentration depends on particle size, not the concentration itself. In this study, we use the
108 airborne-dust PSD observed at 1 m to approximate emission-dust PSD, and use the airborne-dust PSD observed at 3.5 m and
109 the emission-flux PSD derived from the 3.5 m- and 1 m-OPC measurements for additional discussions (Section 4.2).
110 Hereafter, emission-dust PSD approximated using the 1m-OPC airborne-dust PSD is simply referred to as dust PSD, unless
111 otherwise stated.

112 Atmospheric variables, including wind speed, air temperature and humidity at various levels, radiation and precipitation
113 were measured using an automatic weather station. These quantities were sampled at 5-second intervals and their 1-minute
114 averages were recorded (see Section 4.2 for discussions). Two anemometers mounted at 0.53 and 2.16 m measured wind
115 speed. From the atmospheric data, the Obukhov length, L , sensible heat flux, H , and friction velocity, u_* , were derived.² Also
116 measured were soil temperature and moisture.

² Drag-partition theory (Raupach, 1992; Webb et al., 2019) tells that shear stress, $\tau = \rho u_*^2$, is not the same as the shear stress, τ_s , experienced by soil particles, due to roughness sheltering. For JADE, the surface is bare and thus the effect of roughness sheltering is neglected. The saltation fluxes used in this study are measured and do not involve the assumption $\tau = \tau_s$, or otherwise.



117

118 Figure 1. Soil particle-size distribution obtained using Method A and Method B, together with the respective approximations (Model A
119 and Model B).

120 Surface soil samples were taken and soil PSD was analysed in laboratory using Method A and B with a particle size
121 analyser (Microtrac MT3300EX, Nikkiso). In Method A, water was used for sample dispersion with no ultrasonic action. In
122 Method B, sodium hexametaphosphate (HMP) 0.2% solution was used for sample dispersion and 1-minute ultrasonic action
123 of 40 W was applied. Following the convention of sedimentology, the soil is a sandy loam based on the analysis using
124 Method B. Figure 1 shows $p_A(d)$ (soil PSD from Method A) and $p_B(d)$ (soil PSD from Method B) and the corresponding
125 approximations: p_A shows a larger fraction of particles in the range of 30~300 μm , while p_B a larger fraction of particles in
126 the range of 0.1~30 μm .

127 An overview of the JADE data is shown in Figure 2. During the experiment, 12 significant aeolian events were recorded,
128 as marked in the figure. Most of the events occurred under unstable ABL conditions. Several quantities can be used as a
129 measure of ABL stability, but the one used here is the convective scaling velocity, w_* , defined as

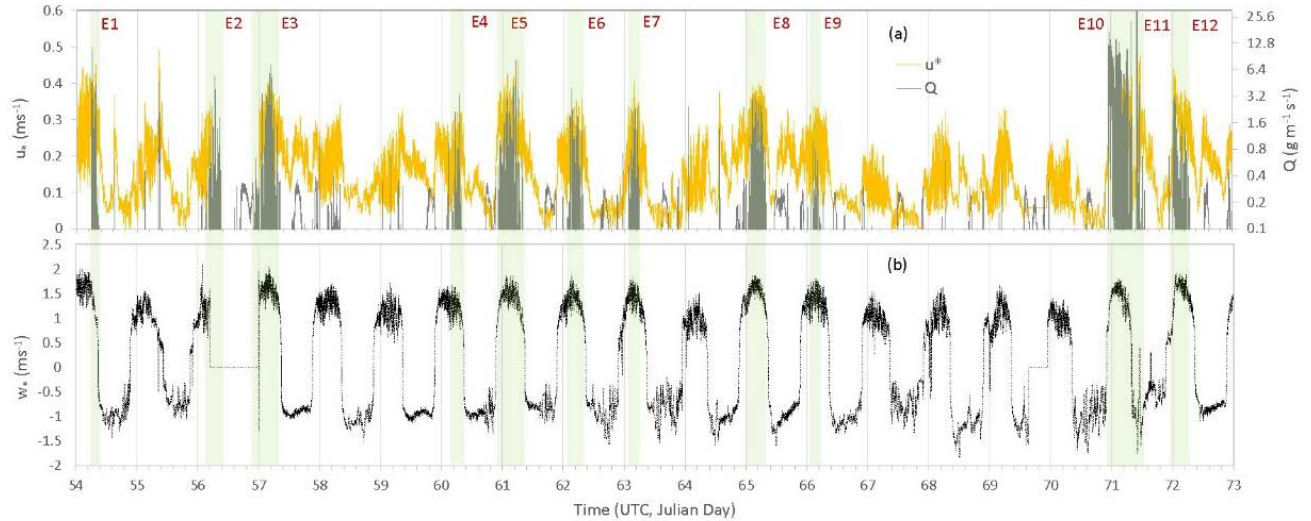
130

$$w_* = \left(\frac{g}{\bar{\theta}} H_0 z_l \right)^{\frac{1}{3}}, \quad (4)$$

131 where $g/\bar{\theta}$ is the buoyancy parameter with g being the acceleration due to gravity and $\bar{\theta}$ the mean potential temperature; H_0 is
132 surface kinematic heat flux (K m s^{-1}) and z_l a scaling length (set to the capping inversion height for convective ABL and 100
133 m for stable ABL). For unstable conditions, w_* is positive while for stable conditions w_* is negative. The reason for choosing
134 w_* is that it is a scaling parameter for the strength of turbulence. Usually, w_* is not used for stable ABLs, but used here as an
135 indicator for the suppression of turbulence by negative buoyancy.

136 In addition to the 12 events, a number of weak and intermittent events occurred. In this study, we first use the whole
137 dataset for the dust PSD analysis, and then use the data for Event-10, 11 and 12 for case studies. These three events are

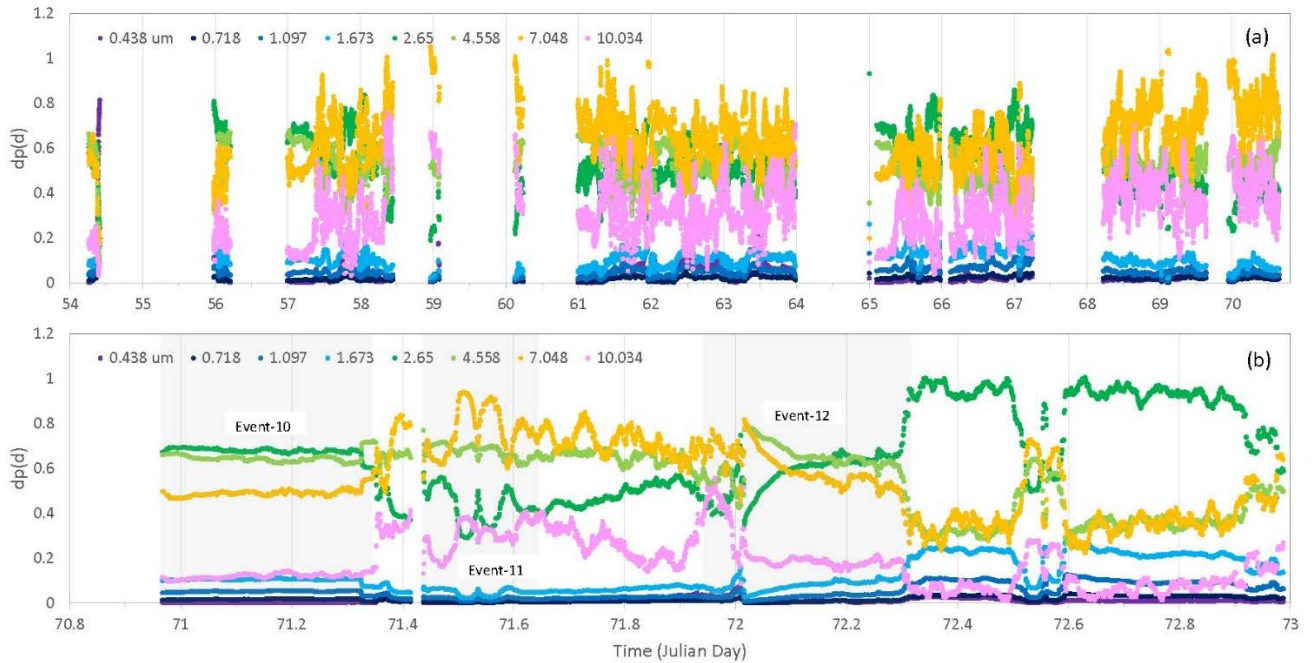
138 chosen for that Event-10 is the strongest event during JADE, Event-11 is one that occurred at night under stable conditions,
139 while Event-12 occurred with a weakly crusted soil surface (Ishizuka et al., 2008).
140



141
142 Figure 2. (a) One-minute averaged friction velocity, u_* , and streamwise saltation flux, Q , for the JADE observation time period; (b) One-
143 minute averaged convective scaling velocity, w_* . In addition to the 12 aeolian events marked, a number of weaker and intermittent aeolian
144 events occurred.

145 3 Results

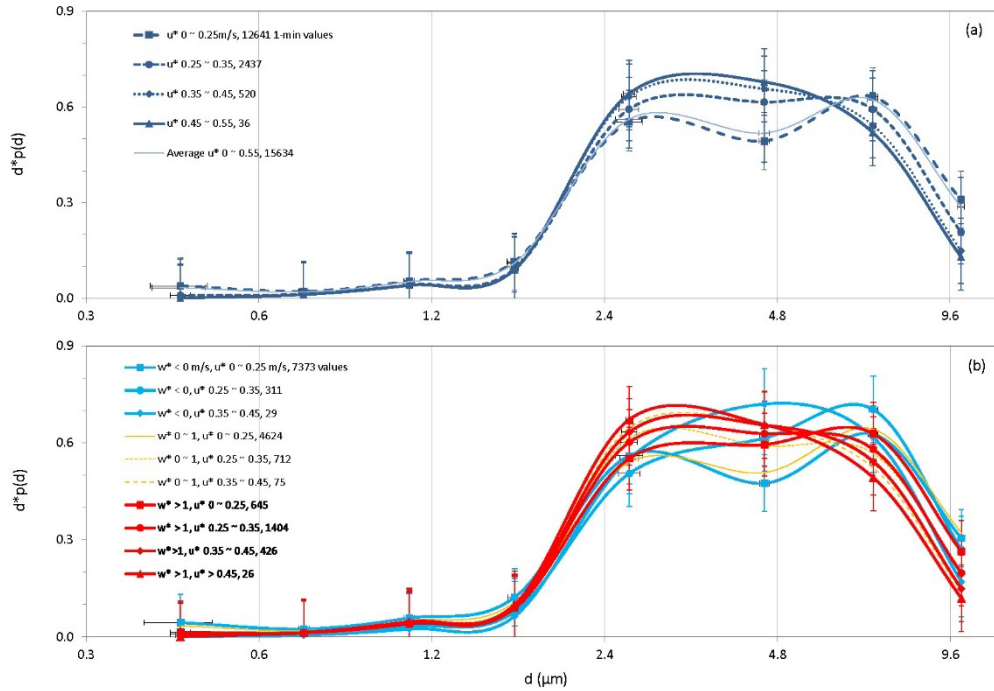
146 3.1 Overall Results



147

148 Figure 3. Dust PSD measured at 1m using OPC for the entire JADE observation period plotted in two sections, (a) for section Julian day
 149 54 ~ 70.8 and (b) for section Julian day 70.8 ~ 73.0.

150 Plotted in Figure 3 are the time series of dust PSD for the entire JADE period, which show rich temporal variations,
 151 probably apart from Event-10. To examine dust-PSD dependency on friction velocity, we use u_* to denote the one-minute
 152 values of friction velocity, $p(u_*)$ its probability density function (PDF), \bar{u}_* its mean and σ_{u_*} its standard deviation. The u_*
 153 values are divided into the categories of 0~0.25, 0.25~0.35, 0.35~0.45 and 0.45~0.55 ms^{-1} , and the corresponding dust PSDs
 154 and saltation PSDs are sorted accordingly. These u_* categories correspond roughly to intermittent, weak, moderate and
 155 strong saltation, respectively. The threshold friction velocity, u_{*t} , for the JADE site is around 0.2 ms^{-1} , but intermittent
 156 saltation has been observed oft at u_* below this u_{*t} . The dust PSDs are then composite averaged for the u_* categories. Figure
 157 4a shows the dust PSDs for the different u_* categories and the mean dust PSD averaged over all u_* categories (including a
 158 total of 15634 one-minute points). We have repeated the same averaging procedure using a subset of the JADE data,
 159 conditioned with $Q > 0.1 \text{ gm}^{-1}\text{s}^{-1}$ and found that the results are very similar to those presented in Figure 4. The mean dust
 160 PSD shows an interesting local minimal at $\sim 4 \mu\text{m}$. This is attributed to the lack of particles of this size in the $u_* < 0.25 \text{ ms}^{-1}$
 161 category. Figure 4a shows that dust PSD clearly depends on u_* , particularly in the size range 2 ~ 10 μm . In general, as u_*
 162 increases, the fraction of fine dust particles increases. For the submicron size range, the dependency of dust PSD on u_* is less
 163 definitive. The dust PSD for the $u_* < 0.25 \text{ ms}^{-1}$ category shows a higher fraction of submicron dust particles, especially in
 164 stable conditions (Figure 4b). Apart from this, the results shown in Figure 4a are consistent with the findings of Alfaro et al.
 165 (1997) that dust PSD is u_* dependent.



166

167 Figure 4. (a) Dust PSD for different u_* categories derived from the whole JADE dataset; (b) as (a), but for the different u_*
 168 categories under stable ($w_* < 0$), moderately unstable ($0 \leq w_* < 1 \text{ ms}^{-1}$) and unstable ($w_* \geq 1 \text{ ms}^{-1}$) conditions.

169

170 To examine the dust PSD dependency on ABL stability, we divide the dataset into stable ($w_* < 0$), moderately unstable (0
 171 $\leq w_* < 1 \text{ ms}^{-1}$) and unstable ($w_* \geq 1 \text{ ms}^{-1}$) stability classes. For each stability class, the dust PSD data are regrouped according
 172 to the u_* categories. Figure 4b shows the dust PSDs averaged for different u_* categories and stability classes. For given
 173 stability class, dust PSD shows dependency on u_* , and for a given u_* category, dust PSD shows dependency on w_* . For given
 174 u_* , the mode of dust PSD shifts systematically to finer particles as the ABL becomes more unstable.

175

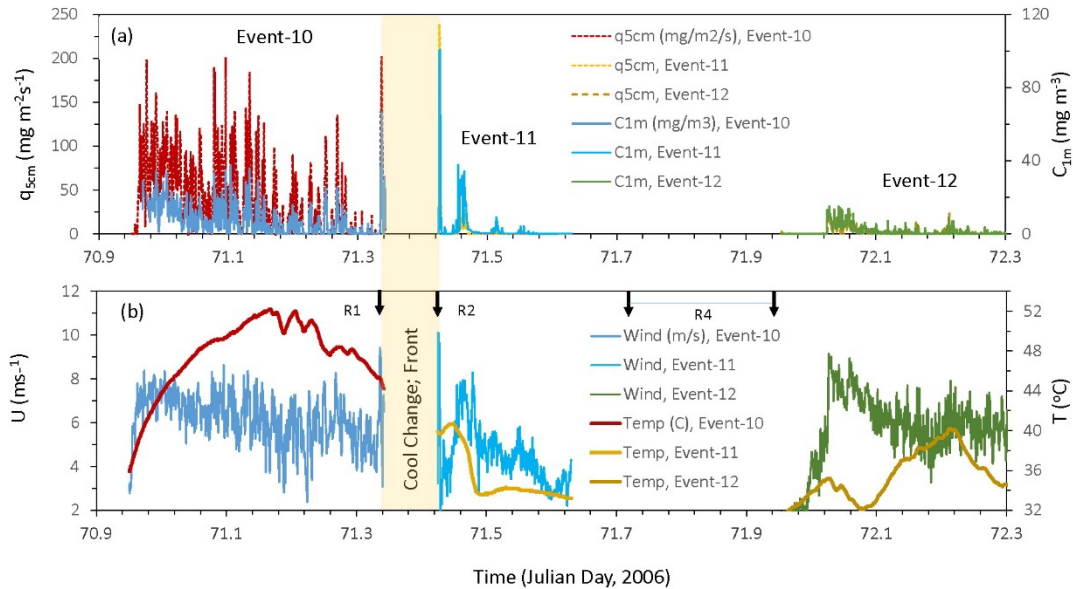
176 3.2 Case Study Results

177 We now study the cases of Event-10 (09:49~19:13 12 Mar 2006; Julian Day 70.9506940~71.3423611), Event-11 (21:12
 178 12 Mar ~ 02:08 13 Mar 2006, Julian Day 71.42500~71.63056) and Event-12 (09:54~18:58 13 Mar 2006, Julian Day
 179 71.95417~72.33194). Figure 5 shows the one-minute averages of wind speed at 0.53 m, U , air temperature at 0.66 m, T ,
 180 saltation flux at 0.05 m, $q_{5\text{cm}}$, and dust concentration (summed over all particle size bins) at 1 m, $C_{1\text{m}}$. Event-10 occurred
 181 under daytime unstable conditions. It was a very hot day prior to a cool change (cold front causing temperature drop but no
 182 rainfall), with near surface air temperature reaching 52°C and wind speed $\sim 8 \text{ ms}^{-1}$. The event lasted ~ 10 hours. The cool
 183 change occurred at $\sim 19:00\text{--}21:00$ 13 Mar 2006 local time. While precipitation was not recorded by the rain gauge (with
 184 resolution of 0.2 mm), the rain sensor [PPS-01(C-PD1), PREDE Co. Ltd.], as marked in Figure 5b, sensed an event of

185 raindrops shortly before the cool change, lasting about two minutes, and shortly after, lasting about one minute (Ishizuka et
 186 al., 2008). The strong winds (probably also strong sand drift and dust emission) accompanying the cool change caused the
 187 shutdown of the instruments and thus, unfortunately, this period was not fully recorded. Event-11 occurred under stable
 188 conditions after the cool change in the night time of 12/13 Mar 2006, during which T was dropping from $\sim 40^{\circ}\text{C}$ to $\sim 33^{\circ}\text{C}$ and
 189 U from $\sim 8\text{ ms}^{-1}$ to $\sim 5\text{ ms}^{-1}$. Event-11, which can also arguably be considered to be part of Event-10, was much weaker than
 190 Event-10.

191 As the OPC measurements were taken close to the surface and directly above the dust source, the dust-concentration
 192 values were generally high. For Event-10, the mean, standard deviation, maximum and minimum of $C_{1\text{m}}$ are respectively
 193 7.56, 8.56, 65.96 and 0.02 mg m^{-3} , and for Event-11 3.05, 10.57, 100.17 and 0.04 mg m^{-3} . The extremely high dust
 194 concentrations measured shortly before and after the cool change could be affected by dust advection and are excluded from
 195 the analysis (although their inclusion made no difference to the event averages of the dust PSDs). For other times, it can be
 196 safely assumed that the dust observed was locally emitted.

197



198

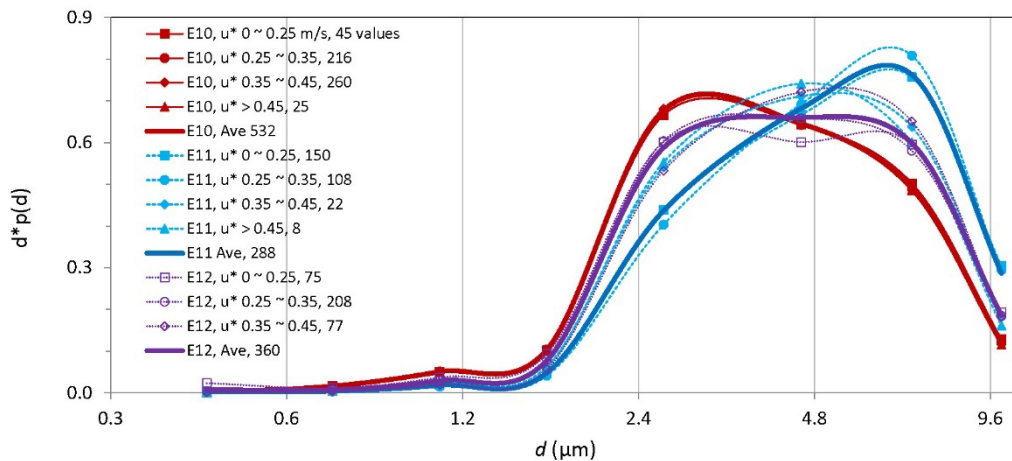
199 Figure 5. (a) one-minute averaged saltation flux at 0.05 m, $q_{5\text{cm}}$, and dust concentration at 1 m, $C_{1\text{m}}$, for Event-10, -11 and 12;
 200 (b) as (a) but for wind speed at 0.53 m above ground, U , and air temperature at 0.66 m, T . The cool change is marked and the
 201 three rain events sensed by the rain sensor are marked as R1, R2 and R4 using the black arrows.

202

203 Event-12 is developed shortly after the weak rainfall event (R4). Again, while precipitation was not recorded by the rain
 204 gauge (i.e. the total rainfall was less than 0.2 mm), the rain sensor reported rain drops during 71.70625~71.95278. Ishizuka
 205 et al. (2008) reported that Event-12 is unique for JADE, because it is the only case when the soil surface was weakly crusted.

206 We will show later how dust PSD can substantially evolve even within one dust event, as soil surface conditions change
 207 (Figure 10).

208



209

210 Figure 6. Dust PSD for different u_* categories for Event-10, 11 and 12. Also shown are the PSDs averaged over all u_* categories for the
 211 individual events.

212 Figure 6 shows the dust PSDs for the different u_* categories for Event-10, 11 and 12. For Event-11 and 12, the
 213 dependency of dust PSD on u_* is obvious, in agreement with the overall results shown in Figure 4a. The dust PSD for Event-
 214 10 shows no clear dependency on u_* , which was reported in Shao et al. (2011). Our basic argument for dust PSD dependency
 215 on u_* rests upon the assumption that saltation-impact speed is u_* dependent. It has been suggested that impact-particle speed
 216 may not strongly depend on u_* for transport-limited saltation (Ungar and Haff, 1987), because particle-flow feedbacks force
 217 an approximately constant saltation-impact speed. While this argument is supported by some experimental evidence (Martin
 218 and Kok, 2017) and numerical simulations (Duran et al., 2012; Kok et al., 2012), its general validity and the conditions for
 219 its validity need further examination. JADE Event-10 is probably a case which comes closest to meet the requirements of
 220 strong particle-flow feedback and sustained equilibrium of saltation for the Ungar and Haff (1987) hypothesis to apply. In
 221 addition, Event-10 occurred on an extremely hot and dry day, with the 0.66 m air temperature reaching $\sim 52^\circ\text{C}$ and relative
 222 humidity below 3%. It is likely that under such extreme conditions, inter-particle cohesion is destroyed. These factors
 223 combined may be responsible for the lack of dust PSD dependency on u_* for Event-10 (Figure 6). But for all other JADE
 224 events, the dependency of dust PSD on u_* is significant.

225 The event-averaged dust PSDs for Event-10, -11 and -12 clearly differ. For Event-10, the mean and standard deviation of
 226 u_* and w_* were respectively (0.36, 0.057) and (1.03, 0.29), all in ms^{-1} , and for Event-11 (0.28, 0.077) and (-0.41, 0.159).
 227 From Event-10 to -11, the dust PSD mode shifted from about $3 \mu\text{m}$ to $6 \mu\text{m}$. During Event-10, a substantially higher fraction
 228 of particles in the size range of $0.4 \sim 4 \mu\text{m}$ existed. To further examine how dust PSD depends on saltation intensity, we have
 229 averaged the dust PSDs for different Q categories (not shown). It is found that weak saltation corresponded to coarser dust

230 particles and strong saltation to finer dust particles. Figure 6 confirms the dependency of dust PSD on ABL stability,
231 consistent with the overall results shown in Figure 4.

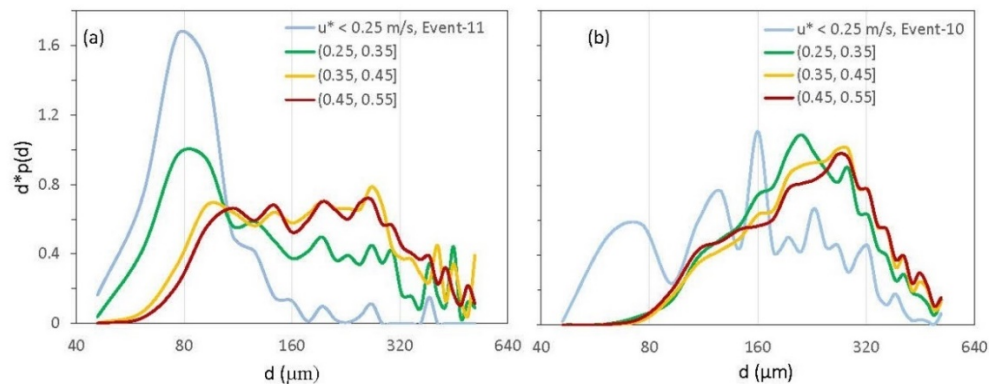
232 Figure 5b shows that the wind conditions for Event-10 and Event-12 were not too different, but Event-12 was much
233 weaker. Figure 6 shows that also the dust PSDs for the two events considerably differ, with Event-10 being the one with
234 richer finer dust particles. Event-12 will be further discussed in Section 4.2.

235 We make the following observations based on the JADE data: (1) Dust PSD has rich temporal variations and is not
236 “universal”; (2) Dust PSD depends on u_* and ABL stability; and (3) Dust PSD is influenced by soil surface conditions. These
237 observations support the conceptual understanding that dust PSD is determined both by saltation bombardment and by soil
238 binding strength (Shao, 2001, 2004).

239 4 Discussions

240 4.1 Influence of Turbulence on dust PSD

241 The reason for the dependency of dust PSD on u_* has been explained in Gillette et al. (1974), Gillette (1981), Shao et al.
242 (1993), Alfaro et al. (1997) and Shao (2001; 2004), because u_* is a descriptor of saltation bombardment intensity. In the
243 earlier explanations, only mean friction velocity and mean saltation are considered, while the turbulent nature of saltation
244 bombardment is implicitly neglected. But how is the dependency of dust PSD on ABL stability, here w_* , explained? The
245 most conspicuous reason is the enhanced saltation bombardment by turbulence in unstable conditions.



246

247 Figure 7. (a) Saltation PSD averaged for four different u_* categories for Event-11; (b) as (a), but for Event-10.

248 It is interesting to examine how dust PSD is related to saltation PSD. The saltation PSD for Event-10 and -11 are shown in
249 Figure 7. First, for $u_* \leq 0.25$ ms^{-1} in Event-11, saltation PSD was confined to a narrow size range centred at 70~80 μm where
250 u_{*t} is minimum. This indicates that saltation splash/bombardment was weak to mobilize particles in other size ranges. In

251 contrast, for $u_* \leq 0.25 \text{ ms}^{-1}$ in Event-10, saltation PSD covered a broader size range, implying that saltation splash was strong
 252 to entrain particles of other sizes. Second, for both Event-10 and -11, the peak values of saltation PSD were shifted to larger
 253 particles for larger u_* : for Event-10 the peak for $0.25 < u_* \leq 0.35 \text{ ms}^{-1}$ was at $203.3 \text{ }\mu\text{m}$, while for $0.45 < u_* \leq 0.55 \text{ ms}^{-1}$ at
 254 $257.8 \text{ }\mu\text{m}$. Clearly, since u_{*t} is particle size dependent, saltation PSD is a selective sample of the soil PSD by wind. Third, the
 255 saltation PSDs for given u_* categories (e.g., $0.35 < u_* \leq 0.45 \text{ ms}^{-1}$, Figure 8a and 8b) differed significantly between Event-10
 256 and -11 as a consequence of ABL stability. In Event-11 (Figure 8a), saltation was not fully developed, as the saltation PSD
 257 plateau in the size range $100\text{--}300 \text{ }\mu\text{m}$ suggests, implying that saltation splash/bombardment was not efficient. In Event-10
 258 (Figure 7b), saltation was more fully developed.

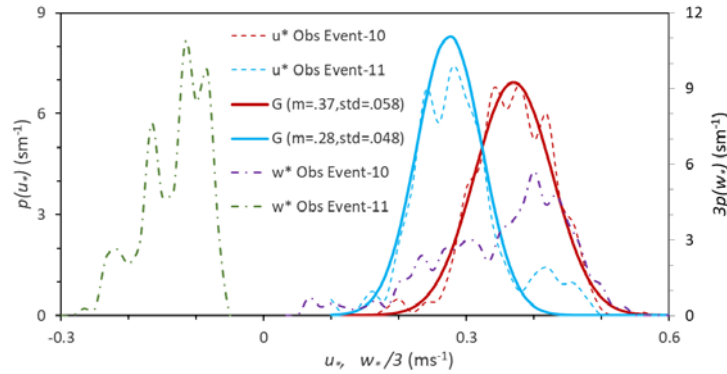
259 The stronger saltation of Event-10 is partially attributed to the stronger wind and instability, which result in a larger \bar{u}_*
 260 than in Event-11. It is known from the ABL similarity theory that,

$$261 \quad \bar{u}_* = \frac{\kappa z}{\phi_m} \frac{\partial \bar{u}}{\partial z}, \quad (5)$$

262 where κ is the von Karman constant, z height and ϕ_m a similarity function (Stull, 1988):

$$263 \quad \phi_m = \begin{cases} 1 + \beta_m \zeta & \zeta > 0 \text{ stable} \\ (1 - \gamma_m \zeta)^{-1/4} & \zeta < 0 \text{ unstable,} \\ 1 & \zeta = 0 \text{ neutral} \end{cases} \quad (6)$$

264 where $\zeta = z/L$ (L is Obukhov length) and $\beta_m = 5$ and $\gamma_m = 16$ are empirical coefficients (Businger et al., 1971). For stable
 265 conditions, $\phi_m > 1$ and for unstable conditions $\phi_m < 1$. Figure 8 shows the PDFs of u_* and w_* for Event-10 and -11,
 266 together with the approximations for the PDFs of u_* . For Event-10, $\bar{u}_* = 0.37 \text{ ms}^{-1}$, while for Event-11, $\bar{u}_* = 0.28 \text{ ms}^{-1}$.



267

268 Figure 8. The probability density functions of u_* and w_* , $p(u_*)$ and $p(w_*)$, respectively, for Event-10 and -11, together with the Gaussian
 269 approximations for the $p(u_*)$ functions. The mean values (m) and standard deviations (std) for the Gaussian (G) distributions are given.
 270 Note that for $p(w_*)$, $3p(w_*)$ against $w_*/3$ is plotted to conveniently present the information in the same graph.

271 We suggest that the dependency of dust PSD on w_* for given u_* is attributed to saltation bombardment intensity from two
 272 perspectives. First, as Figure 8 shows, u_* is a stochastic variable. Li et al. (2020) suggested that $\tau = \rho u_*^2$ in neutral conditions
 273 is Gauss distributed. Klose et al. (2014) reported that τ in unstable conditions is Weibull distributed. The exact form of $p(\tau)$
 274 requires further investigation, but the JADE data of u_* show that $p(u_*)$ is reasonably Gaussian. Hence,

$$275 \quad p(\tau) = \frac{1}{2\rho u_*} p(u_*), \quad (7)$$

276 is skewed to smaller τ , suggesting that the large-eddy model results of Klose et al. (2014) are qualitatively reasonable. Figure
 277 8 shows that u_* in Event-10 not only had a larger mean value but also a larger variance than in Event-11. We emphasize that
 278 the variance of u_* strongly affects saltation, because saltation flux depends non-linearly on u_* . To illustrate this, we consider
 279 u_{*1} and u_{*2} , and assume that

- 280 • u_{*1} and u_{*2} are Gaussian distributed and have the same mean that equals u_{*i} (say 0.2 ms⁻¹)
- 281 • u_{*1} and u_{*2} have respectively standard deviation, σ_1 and σ_2 , with $\sigma_2 = \eta \sigma_1$ and $\eta > 1$; and
- 282 • Q satisfies the Owen's model (Owen, 1964),

$$283 \quad Q_i = c u_{*i}^3 \left(1 - \frac{u_{*t}^2}{u_{*i}^2} \right) \quad \text{for } u_* > u_{*t};$$

$$284 \quad \text{otherwise } 0; \quad \text{with } i = 1, 2, \quad (8)$$

285 where c is a dimensional constant. It follows that the ratio of the mean values of Q_2 and Q_1 is

$$286 \quad \eta_Q = \frac{\bar{Q}_2}{\bar{Q}_1} = \int_{u_{*t}}^{\infty} Q_2 p(u_{*2}) du_{*2} / \int_{u_{*t}}^{\infty} Q_1 p(u_{*1}) du_{*1}, \quad (9)$$

287 Equation (9) can be evaluated numerically for different η (Table 1) and is approximately

$$288 \quad \eta_Q = 0.607 \eta^2 - 0.0028\eta + 0.4283, \quad (10)$$

289 This shows that $p(u_*)$ profoundly influences the magnitude of Q . For fixed \bar{u}_* , a larger u_* variance corresponds to a larger \bar{Q} .

290 Table1. Streamwise saltation flux ratios, η_Q , for different u_* std ratios, η (see text for details).

η	1.2	1.4	1.6	1.8	2	3	4
η_Q	1.30	1.63	2.00	2.41	2.86	5.83	10.15

291 Second, in unstable conditions, turbulence is stronger due to buoyancy production, which leads to increased saltation
 292 bombardment intensity. We do not have independent evidence to verify this, but to illustrate the point, we use a two-
 293 dimensional (2-d, x_1 in mean wind direction and $x_3 \equiv z$ in vertical direction) saltation model (Supplement A) to simulate the

294 impact kinetic energy of saltation sand grains. For given u_* and roughness length, z_0 , a 2-d turbulent flow is generated with
 295 the mean wind assumed to be logarithmic $\overline{\kappa u_1} = \overline{u_*} \ln(z/z_0)$ and the velocity standard deviations satisfy

296
$$\frac{\sigma_{u1}}{\overline{u_*}} = a \cdot \ln\left(\frac{z}{z_0}\right), \quad (11)$$

297
$$\frac{\sigma_{u3}}{\overline{u_*}} = f_{u3}(\zeta) \cdot a \cdot \ln\left(\frac{z}{z_0}\right), \quad (12)$$

298 and the dissipation rate for turbulent kinetic energy, ε , satisfies

299
$$\varepsilon \frac{\kappa z}{\overline{u_*}^3} = f_\varepsilon(\zeta), \quad (13)$$

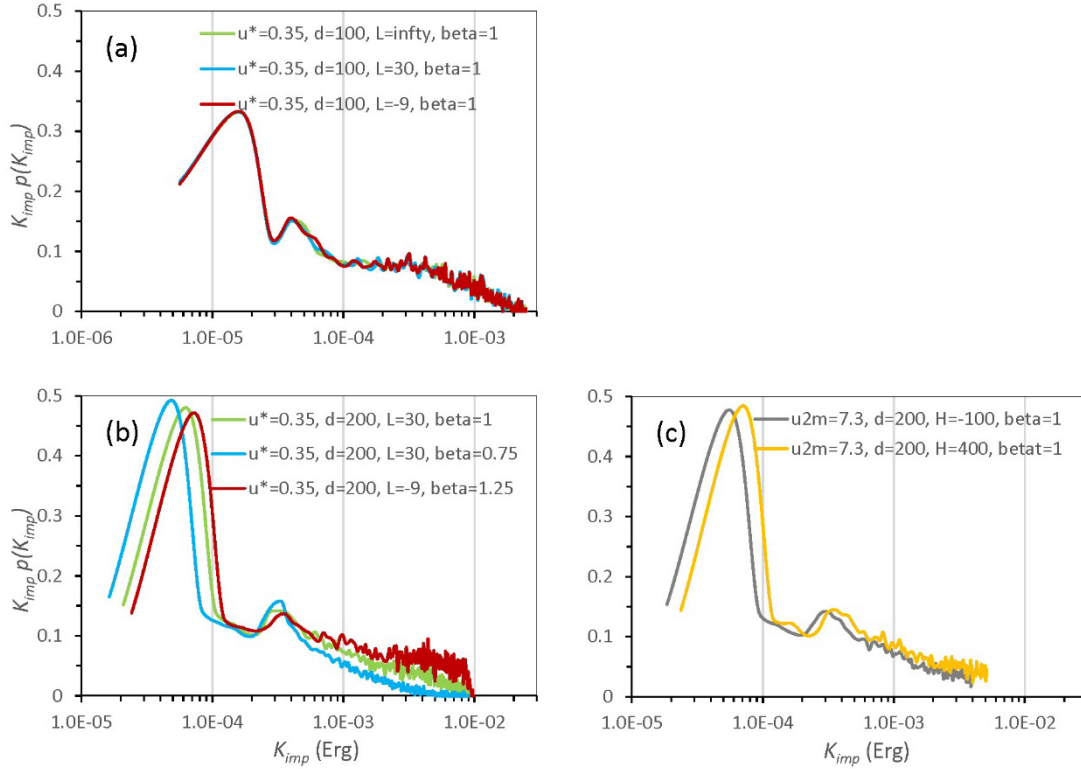
300 The similarity relationships $f_{u3}(\zeta)$ and $f_\varepsilon(\zeta)$ follow Kaimal and Finnigan (p16, 1995). As saltation takes place in the layer
 301 close to the surface, the vertical profiles of σ_{u1} and σ_{u3} are considered following Yahaya et al. (2003). The coefficient a
 302 ($=1.16\beta$) is varied by setting β to 0.75, 1.00 and 1.25 for weak, normal and strong turbulence, respectively.

303 In each numerical experiment, 20000 sand grains of identical size are released from the surface and their trajectories are
 304 computed. At impact on the surface, the particles rebound with a probability of 0.95 and a rebounding kinetic energy, K_{reb} ,
 305 0.5 times the impact kinetic energy, K_{imp} . The rebound angle is Gauss distributed with a mean of 40° and standard deviation
 306 5° . Splash entrainment is neglected. The PDF of K_{imp} , $p(K_{imp})$, is used as a measure for bombardment intensity.

307 Many numerical experiments were carried out, but for our purpose, we show only the results of the ones listed in Table 2.
 308 The initial velocity components of sand grains (V_{1o} , V_{3o}) are generated stochastically. V_{1o} is Gauss distributed with a mean
 309 $\overline{V}_{1o} = \overline{u_*} \cos(55^\circ)$ and standard deviation, $\sigma_{V_{1o}} = 0.1\overline{u_*}$. V_{3o} is Weibull distributed with a shape parameter $A = 2$ and a scale
 310 parameter $B' = \overline{u_*} \sin(55^\circ) / \Gamma(1 + 1/A)$ where Γ is a Gamma function. To account for the influence of stability on V_{3o} , B'
 311 is modified such that the adjustment to $\sigma_{V_{3o}}$ is the same as that to $\sigma_{u3}(10z_0)$, i.e., the modified scale parameter, B , is given
 312 by

313
$$B = \beta f_{u3}\left(\frac{10z_0}{L}\right) B'. \quad (14)$$

314



315

316 Figure 9. Probability density function $p(K_{imp})$ (plotted in $K_{imp}p(K_{imp})$ against K_{imp} in logarithmic scale) for the numerical experiments. In
 317 (a), $p(K_{imp})$ is shown for $u_* = 0.35\text{ms}^{-1}$, $d = 100\mu\text{m}$ and $\beta = 1$ but for three different Obukhov lengths $L = \infty, 30\text{m}$ and -9m . In (b), the effect
 318 of β on $p(K_{imp})$ is examined; and in (c) the effect of stability on $p(K_{imp})$ with given mean wind speed at $z = 2\text{m}$ is examined.

319 Figure 9a compares $p(K_{imp})$ for Exp1a, 1b and 1c and shows that $p(K_{imp})$ for these cases is very similar. The small
 320 differences in $p(K_{imp})$ between the cases suggest that the differences in particle trajectory arising from the stability
 321 modification to turbulence profile, with u_* fixed, are negligible. However, a small change in β , as Figure 9b shows for Exp2a,
 322 2b and 2c, can lead to significant changes in $p(K_{imp})$ with larger β corresponding to higher probability of larger K_{imp} , namely,
 323 high saltation bombardment intensity. In Exp3a and 3b, u_{2m} (mean wind 2m height) is set to 7.3ms^{-1} and the surface sensible
 324 heat flux, H , to -100 and 400Wm^{-2} . Figure 9c shows that $p(K_{imp})$ differs with larger K_{imp} in unstable conditions.

325 Table 2: Numerical experiments for saltation bombardment intensity. For all experiments, $z_0 = 0.48\text{mm}$, $C_0 = 5$, $C_1 = 2$ and $\rho_p = 2650\text{kgm}^{-3}$.

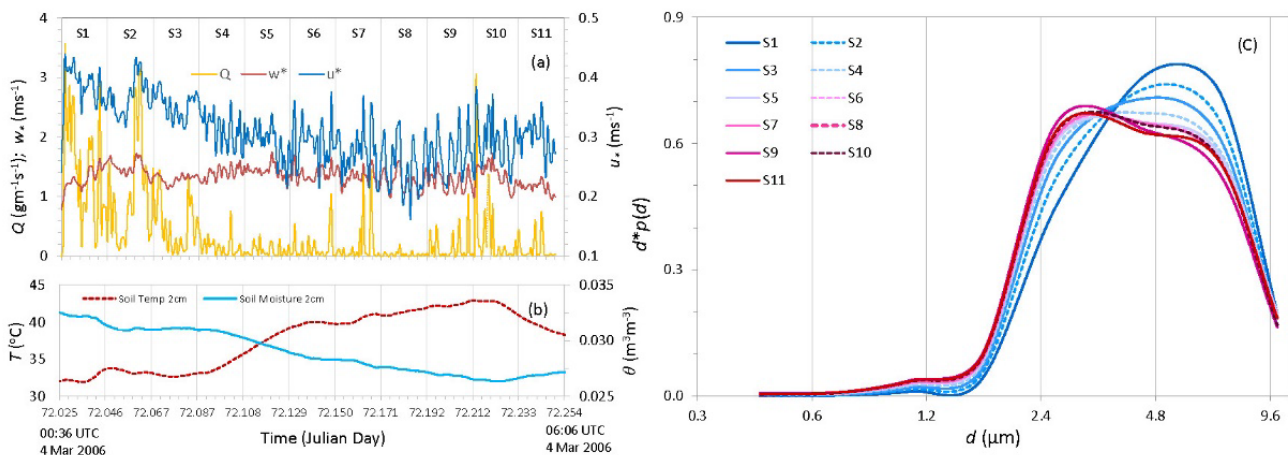
Exp	u_* (ms^{-1})	L (m)	d (μm)	β
Exp1a, 1b, 1c	0.35	$\infty, 30, -9$	100	1.0
Exp2a, 2b	0.35	30	200	0.75, 1
Exp2c	0.35	-9	200	1.25
Exp3a, 3b	$u_{2m}=7.3$	$H=-100; 400\text{Wm}^{-2}$	200	1

326

327 To summarize, the numerical experiments suggest that the PDF of the particle initial velocity significantly influences the
 328 saltation bombardment intensity, and saltating particles in unstable ABL impact the surface with larger kinetic energy than in
 329 stable ABL. This is the result seen in Figure 7 and 8, i.e., saltation in Event-10 was more fully developed than in Event-11.
 330 The more fully developed saltation in unstable ABL increases saltation bombardment intensity and hence the release of finer
 331 dust particles, seen in Figure 6.

332 4.2 Influence of Surface Condition on Dust PSD

333 A detailed analysis of Event-12 (Figure 10) reveals that the dependency of dust PSD on friction velocity and ABL stability
 334 is made complicated by soil surface conditions. To analysis how dust PSD evolved during the event, we divide Event-12
 335 which lasted ~5.5 hours, into 11 half-hourly time sections labelled as S1, S2 etc. For each section, the dust PSD is averaged
 336 over time and plotted in Figure 10c. Figure 10a shows the time series of Q , w_* and u_* , and Figure 11b those of 2 cm soil
 337 temperature and soil moisture. For the whole event, the ABL was unstable, with w_* fluctuating around $1.64 \pm 0.12 \text{ ms}^{-1}$.
 338 Initially (e.g. S1 and S2), u_* was relatively large, exceeding 0.4 ms^{-1} at times, but then eased to around 0.3 ms^{-1} . Q generally
 339 followed the variations of u_* . Yet, the dust PSD showed a systematic shift from coarser to finer particles, as the event
 340 progressed. The dust PSD dependency on u_* of Event-12 does not conform with the results for Event-11 (Figure 6) and the
 341 overall results (Figure 4a). Ishizuka et al. (2008) noticed that prior to Event-12, weak rainfall occurred (R4, Figure 5b) and
 342 consequently, weak crusts formed on the soil surface. Apparently, the lightly crusted surface prevented the emission of fine
 343 dust particles in the early stages of Event-12. As the event progressed, soil temperature increased, soil moisture decreased
 344 (Figure 10b) and the saltation during the early stages caused the destruction of the crusts and the amount of fine dust
 345 particles available for emission increased. These are the most likely reasons for why in the later stages of Event-12, an
 346 increased fraction of fine dust was released, although the atmospheric stability did not significantly change and u_* actually
 347 decreased.



348

349 Figure 10. (a) Time series of streamwise saltation flux, Q ($\text{gm}^{-1}\text{s}^{-1}$), convective scaling velocity, w_* (ms^{-1}), and friction velocity, u_* (ms^{-1}),
350 for Event-12. The time span of Event-12 is divided into 11 half-hourly sections, labelled as S1, S2 etc. (b) As (a), but for soil temperature,
351 T ($^{\circ}\text{C}$), and soil moisture, θ (m^3m^{-3}), both at 0.02m depth. (c) Dust PSDs averaged over section S1, S2 etc.

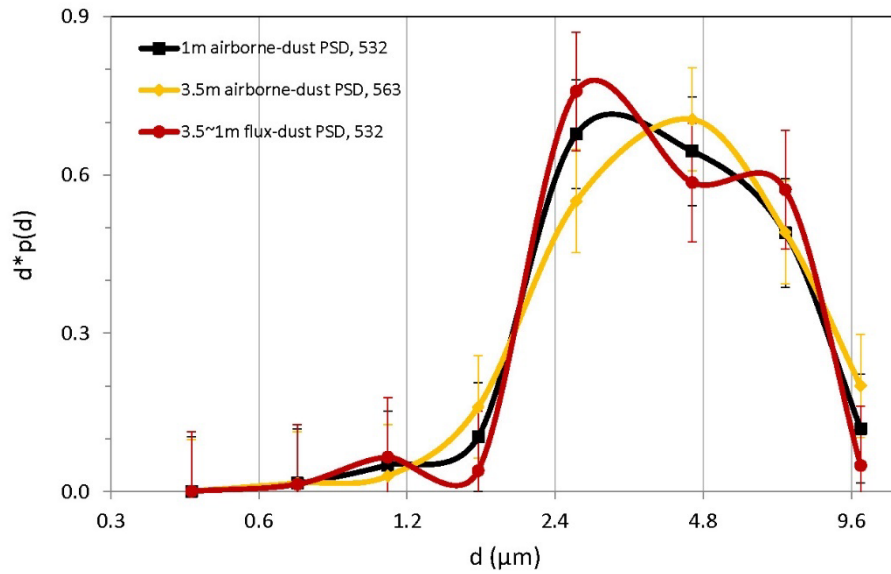
352

353 4.3 Uncertainties

354 Several issues are related to the uncertainties of the analysis. First, the approximation of emission-dust PSD with airborne-
355 dust PSD measured at some height above ground causes uncertainties, because airborne-dust PSD is height dependent as
356 consequence of the dust-transport processes (e.g. diffusion and deposition) in the atmosphere, which are both particle-size
357 and turbulence-property dependent. As our understanding of these processes is not complete and dust measurements have
358 inaccuracies, a careful selection of the data for the analysis is necessary. Figure 11 shows a comparison of Event-10
359 averaged airborne-dust PSDs at 1 m and 3.5 m. Ishizuka et al. (2014) suggested to exclude the 2m-OPC data, because they
360 do not correlate well with the 1 m- and 3.5 m-OPC data. The PSDs derived from the 2m-OPC data do show unexpected
361 differences in comparison to those from the 1m- and 3.5m-OPC data. We thus have excluded the 2m-OPC data from our
362 analysis. The PSDs derived from the 1m- and 3.5m-OPC data somewhat differ, with the peak particle size shifted by about
363 two microns, i.e., airborne-dust PSD has a noticeable change with height. This also implies that it would be very difficult to
364 compare airborne-dust PSD measured at different locations and under different conditions without a well-established
365 framework equivalent to the Monin-Obukhov similarity theory.

366 Also shown in Figure 11 is the Event-10 averaged emission-flux PSD calculated using Equation (3a). Dust fluxes for
367 different particle size bins are calculated using the 3.5m- and 1m-OPC data with the gradient method (Gillette et al. 1972)
368 and corrections (Shao et al. 2011). As dust flux is proportional to the negative gradient of dust concentration, emission-flux
369 PSD basically describes how dust-concentration gradient [in our case $-(c_{3.5\text{m}} - c_{1\text{m}})$] depends on particle size.

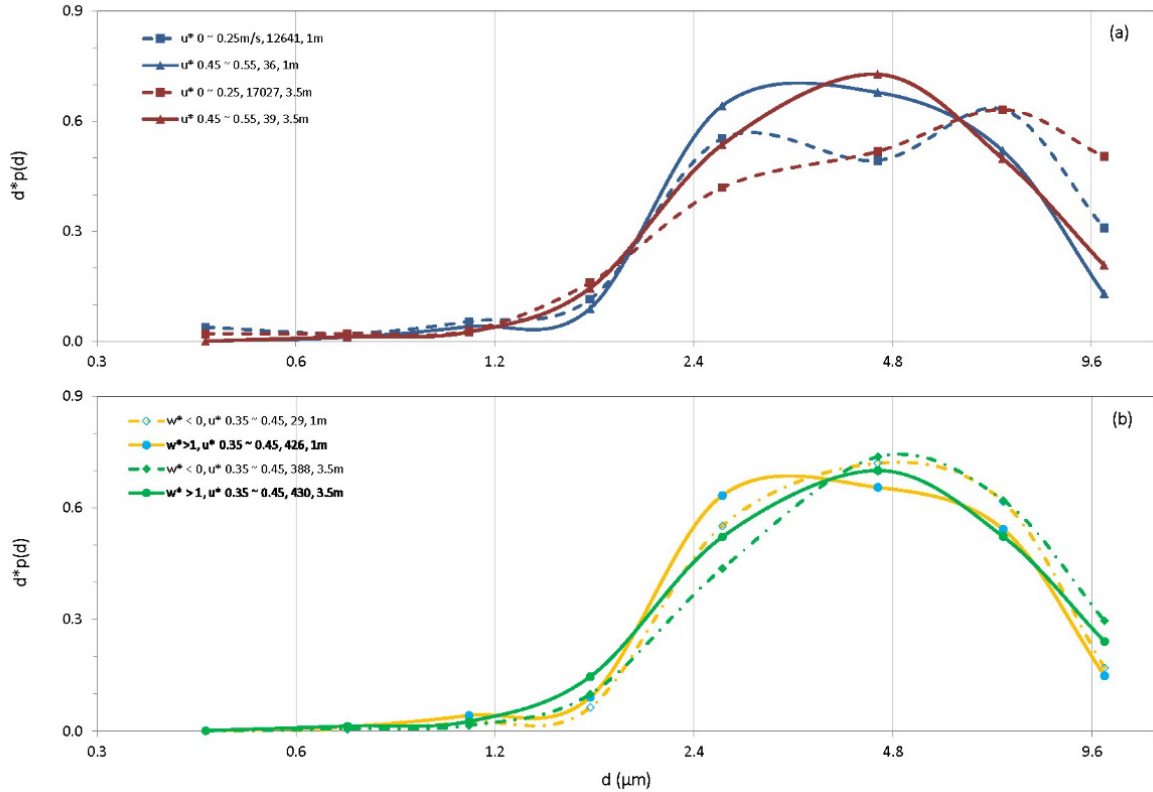
370



371

372 Figure 11: JADE Event-10 averaged airborne-dust PSD measured at 1m (532 one-minute samples) and 3.5m (563 one-
 373 minute samples) using OPCs. Also shown are standard-error bars. For comparison, Event-10 averaged (over 532 one-minute
 374 samples) emission-flux PSDs calculated using Equation (3a) is plotted.

375 Although dust PSDs derived from 1m-OPC and 3.5m-OPC data differ, qualitatively they show similar dependencies of
 376 dust PSD on u_* and w_* . Figure 12a compares the averaged dust PSDs for two u_* categories using the 1m-OPC and 3.5m-OPC
 377 data. For both cases, the dust PSD dependency on u_* is visible. Figure 12b compares the averaged dust PSD for a given u_*
 378 category ($0.35 \sim 0.45 \text{ ms}^{-1}$) under stable and unstable conditions. Again, both the 1m-OPC and 3.5m-OPC dust PSDs show
 379 dependency on w_* .



380

381 Figure 12: (a) JADE averaged airborne-dust PSD measured at 1 and 3.5m for two u_* categories. (b) As (a) but for one u_*
 382 category and two different stabilities.

383

384 It needs to be clarified whether using 1-minute averages of shear stress, saltation flux and dust flux are appropriate for the
 385 study. Related to this question are two inter-wined yet somewhat different scaling issues, namely, (1) the scaling of turbulent
 386 flux and the corresponding mean variable of boundary-layer turbulent flows (i.e. the flux-gradient relationship); and (2) the
 387 scaling of aeolian fluxes and atmospheric forcing (i.e. saltation/dust-emission intermittency). It is usual in boundary-layer
 388 meteorology to compute a turbulent flux from the profile of the corresponding mean quantity, e.g., mean shear stress from
 389 mean wind profile, and the time interval for the mean is typically 15 to 30 minutes such that the assumptions of horizontal
 390 homogeneity and stationarity commonly made in boundary-layer studies are met. This issue is not yet fully resolved even in
 391 boundary-layer studies. For example, large-eddy models (with spatial resolution of several meters and temporal resolution of
 392 seconds) frequently use the Monin-Obukhov similarity functions to estimate sub-grid surface stress from the grid-resolved
 393 speed. In this study, we distinguish the 1-min averages of u_* from the mean shear stress of the boundary-layer flow to
 394 emphasize the importance of shear stress fluctuations. The problem how to scale aeolian fluxes is not new (e.g. Shao and
 395 Mikami, 2005). Dupont (2020) has a dedicated paper on this problem and stated that u_* is a suitable scaling parameter for
 396 dust flux over usual 15~30-min time intervals, but at smaller time resolution, wind becomes more relevant to scale dust

397 fluxes, a conclusion similar to that reached in Sterk et al. (1998). The studies of Stout and Zobeck (1997) and Sterk et al.
398 (1998), and more recently Klose and Shao (2012) and Klose et al. (2014), all pointed to the importance of taking
399 instantaneous shear stress into consideration of aeolian dynamics. As Shao (2008, p203-205) explains, τ_{inst} is proportional to
400 U'^2 , where τ_{inst} is instantaneous shear stress and U' instantaneous wind speed. The argument of Shao (2008) reasonably well
401 explains the conclusions of Sterk et al. (1998) and Dupont (2020). Liu et al. (2018, Figure 7) analysed co-spectrum of
402 saltation flux and shear stress and showed that they have a correlation peak at 2×10^{-3} Hz, corresponding to gusts/large eddies
403 of around 10 minutes in turbulent flows. These considerations suggest that to average shear stress and aeolian fluxes over
404 one minute is appropriate and has the advantage of showing how dust emission is related to turbulence. We have emphasised
405 throughout this paper that turbulence is key to understanding the dependency of dust PSD on ABL stability, because the
406 most essential difference among ABLs of different stability are the intensity and structure of turbulence.

407 As far as averaged dust PSDs are concerned, we have compared the dust PSDs averaged for different u_* categories using
408 1-minute averaged data and 10-minute averaged data. The results are almost the same.

409 5 Conclusions

410 Using JADE data, we showed that dust PSD is dependent on friction velocity u_* . This finding is consistent with the wind-
411 tunnel study of Alfaro et al. (1997). The JADE data support the claim that dust PSD is saltation-bombardment dependent and
412 does not support the hypothesis that dust PSD is invariant.

413 The JADE data show that dust PSD, as well as saltation PSD, also depends on ABL stability. This finding is consistent
414 with the results of Khalfallah et al. (2020). Dust PSD is dependent on ABL stability for two reasons. First, u_* is a stochastic
415 variable and the PDF of u_* profoundly influences the magnitude of saltation flux, Q , because of the non-linear relationship
416 between Q and u_* . With fixed u_* mean, a larger u_* variance corresponds to a larger Q . Unstable ABL has in general larger u_*
417 variances which generate stronger saltation bombardment and produce the emission of finer dust particles. Second, in
418 unstable ABL, turbulence is generally stronger and in strong turbulent flows, the proportion of saltation particles with large
419 impacting kinetic energy is larger than in weak turbulent flows. Consequently, saltation in unstable ABLs is more fully
420 developed and saltation bombardment has higher intensity.

421 The dependencies of dust PSD on u_* and ABL stability are ultimately attributed to the statistic behaviour of u_* , i.e., its
422 PDF $p(u_*)$, or more simply its mean and variance. These dependencies point to the same fact that, for a given soil, saltation
423 bombardment plays a determining role for the dust PSD. Stronger saltation causes in general the emission of finer dust.

424 The dependency of dust PSD on u_* and ABL stability is made complicated by soil surface condition. In the case of strong
425 saltation and very weak surface/particle binding, the dust PSD dependency on u_* may become less obvious. In the case of
426 strong surface/particle binding, dust emission in certain size ranges may be prohibited.

427
428 *Data availability.* Data can be accessed by contacting the corresponding authors.

430 *Author contributions.* Yaping Shao performed the data analyses and drafted the manuscript. Jie Zhang and Ning Huang
431 contributed to the conception of the study, the data analysis and the writing of the manuscript. Masahide Ishizuka, Masao
432 Mikami and John Leys conceived, designed and performed the experiments and helped finalize the paper.

433

434 *Competing interests.* The authors declare that they have no conflict of interest.

435

436 *Acknowledgments.* We thank the National Key Research and Development Program of China (2016YFC0500901), the
437 National Natural Foundation of China (11602100, 11172118) and the Fundamental Research Funds for the Central
438 Universities (lzujbky-2020-cd06) for support. The JADE project was supported by Kakenhi, Grants-in-Aid for Scientific
439 Researches (A) from the Japan Society for the Promotion of Science (Nos. 17201008 and 20244078) and the Lower Murray-
440 Darling Catchment Management Authority. We are grateful to the three referees for their constructive comments and to Dr.
441 Sylvain Dupont and Dr. Jasper Kok for helpful discussions.

442 **References**

443 Albani, S., Mahowald, N. M., Perry, A. T., Scanza, R. A., Zender, C. S., Heavens, N. G., Maggi, V., Kok, J. F. and Otto-
444 Bliesner, B. L., Improved dust representation in the Community Atmosphere Model. *J. Adv. Model. Earth Syst.*, 6, 541–
445 570, doi:10.1002/2013MS000279, 2014.

446 Alfaro, S. C., Gaudichet, A., Gomes, L. and Maille, M., Modeling the size distribution of a soil aerosol produced by
447 sandblasting. *J. Geophys. Res-Atmos.*, 102: 11239-11249, <https://doi.org/10.1029/97JD00403>, 1997.

448 Astrom, J. A., Statistical models of brittle fragmentation. *Adv. Phys.*, 55, 247-278, <https://doi.org/10.1080/00018730600731907>, 2006.

450 Businger, J. A., Wyngaard, J. C., Izumi, J. and Bradley, E. F., Flux-Profile Relationships in the Atmospheric Surface Layer,
451 *J. Atmospheric Sci.*, 28(2), 181–189, [https://doi.org/10.1175/1520-0469\(1971\)028<0181:FPRITA>2.0.CO;2](https://doi.org/10.1175/1520-0469(1971)028<0181:FPRITA>2.0.CO;2), 1971.

452 Csanady (1963, Turbulent Diffusion of Heavy Particles in the Atmosphere. *J. Atmos. Sci.* 20, 201–208).Csanady, G. T.,
453 Turbulent Diffusion of Heavy Particles in the Atmosphere. *J. Atmos. Sci.*, 20, 201–208, [https://doi.org/10.1175/1520-0469\(1963\)020<0201:TDOHPI>2.0.CO;2](https://doi.org/10.1175/1520-0469(1963)020<0201:TDOHPI>2.0.CO;2), 1963.

455 Dupont, S., Scaling of dust flux with friction velocity: time resolution effects. *J. Geophys. Res-Atmos.*, 125, e2019JD031192,
456 <https://doi.org/10.1029/2019JD031192>, 2020.

457 Durána, O., Andreotti, B. and Claudin, P., Numerical simulation of turbulent sediment transport, from bed load to
458 saltation. *Physics of Fluids*, 24(10), 709-737, <https://doi.org/10.1063/1.4757662>, 2012.

459 Gillette, D. A., Blifford, I. H. and Fenster, C. R., Measurements of aerosol size distributions and vertical fluxes of aerosols
460 on land subject to wind erosion. *J. Appl. Meteor.*, 11, 977-987, [https://doi.org/10.1175/1520-0450\(1972\)011<0977:MOASDA>2.0.CO;2](https://doi.org/10.1175/1520-0450(1972)011<0977:MOASDA>2.0.CO;2), 1972.

462 Gillette, D. A., Blifford, I. H. and Fryrear, D. W., Influence of wind velocity on size distributions of aerosols generated by
463 wind erosion of soils. *J. Geophys. Res.*, 79, 4068-4075, <https://doi.org/10.1029/JC079i027p04068>, 1974.

464 Gillette, D. A., Production of dust that may be carried great distances. *Geol. Soc. Am.*, 186, 11 – 26,
465 <https://doi.org/10.1130/SPE186-p11>, 1981.

466 Giorgi, F., Coppola, E., Solmon, F., Mariotti, L., Sylla, M. B., Bi, X., Elguindi, N., Diro, G. T., Nair, V., Giuliani, G.,
467 Turuncoglu, U. U., Cozzini, S., Güttler, I., O'Brien, T. A., Tawfik, A. B., Shalaby, A., Zakey, A. S., Steiner, A. L., Stordal,
468 F., Sloan, L. C. and Brankovic, C., RegCM4: model description and preliminary tests over multiple CORDEX domains.
469 *Clim. Res.*, 52, 7–29. doi: 10.3354/cr01018, 2012. Ishizuka, M., Mikami, M., Leys, J. F., Yamada, Y., Heidenreich, S.,
470 Shao, Y. and McTainsh, G. H., Effects of soil moisture and dried raindroplet crust on saltation and dust emission. *J.*
471 *Geophys. Res-Atmos.*, 113, D24212, <https://doi.org/10.1029/2008JD009955>, 2008.

472 Ishizuka, M., Mikami, M., Leys, J., Yamada, Y., Heidenreich, S., Shao, Y. and McTainsh G. H., Effects of soil moisture and
473 dried raindroplet crust on saltation and dust emission. *J. Geophys. Res-Atmos.*, 113 (D24),
474 <https://doi.org/10.1029/2008JD009955>, 2008.

475 Ishizuka, M., Mikami, M., Leys, J. F., Shao, Y., Yamada, Y. and Heidenreich, S., Power law relation between size-resolved
476 vertical dust flux and friction velocity measured in a fallow wheat field. *Aeolian Research*, 12, 87–99,
477 <https://doi.org/10.1016/j.aeolia.2013.11.002>, 2014.

478 Kaimal, J. C. and Finnigan J. J., Atmospheric Boundary Layer Flows: Their Structure and Measurements. *Bound.-Lay.*
479 *Meteorol.*, 72, 213–214, <https://doi.org/10.1007/BF00712396>, 1995.

480 Khalfallah, B., Bouet, C., Labiadh, M., Alfaro, S., Bergametti, G., Marticorena, B., Lafon, S., Chevaillier, S., Féron, A.,
481 Hease, P., Henry-des-Tureaux, T., Sekrafi, S., Zapf, P. and Rajot, J. L., Influence of atmospheric stability on the size-
482 distribution of the vertical dust flux measured in eroding conditions over a flat bare sandy field. *J. Geophys. Res-Atmos.*,
483 125, e2019JD031185. <https://doi.org/10.1029/2019JD031185>, 2020.

484 Klose, M. and Shao, Y., Stochastic parameterization of dust emission and application to convective atmospheric conditions.
485 *Atmos. Chem. Phys.*, 12(1), 3263-3293, <https://doi:10.5194/acp-12-7309-2012>, 2012.

486 Klose, M., Shao, Y., Li, X., Zhang, H., Ishizuka, M., Mikami, M. and Leys, J. F., Further development of a parameterization
487 for convective turbulent dust emission and evaluation based on field observations. *J. Geophys. Res-Atmos.*, 119, 10,441–
488 10, <https://doi.org/10.1002/2014JD021688>, 2014.

489 Kok, J. F., Does the size distribution of mineral dust aerosols depend on the wind speed at emission? *Atmos. Chem. Phys.*,
490 11, 10149-10156, <https://doi.org/10.5194/acp-11-10149-2011>, 2011a.

491 Kok, J. F., A scaling theory for the size distribution of emitted dust aerosols suggests climate models underestimate the size
492 of the global dust cycle. *Proc. Natl. Acad. Sci. USA*, 108(3), 1016-1021. <https://doi.org/10.1073/pnas.1014798108>, 2011b.

493 Kok, J. F., Parteli, E. J., Michaels, T. I. and Karam, D. B., The physics of wind-blown sand and dust. *Reports on Progress in*
494 *Physics Physical Society*, 75(10), 106901, <https://doi.org/10.1088/0034-4885/75/10/106901> , 2012.

495 Laurent, B., Marticorena, B., Bergametti, G., Mei, F., Modeling mineral dust emissions from Chinese and Mongolian deserts.
496 *Global Planet Change*, 52: 121–141, <https://doi.org/10.1016/j.gloplacha.2006.02.012>, 2006.

497 Li, G., Zhang, J., Herrmann, H. J., Shao, Y. and Huang, N., Study of aerodynamic grain entrainment in aeolian transport.
498 *Geophys. Res. Lett.*, 47, e2019GL086574, <https://doi.org/10.1029/2019GL086574>, 2020.

499 Liu, D., Ishizuka, M., Mikami, M., and Shao, Y., Turbulent characteristics of saltation and uncertainty of saltation model
500 parameters, *Atmos. Chem. Phys.*, 18, 7595–7606, <https://doi.org/10.5194/acp-18-7595-2018>, 2018.

501 Lu, H. and Shao, Y., A new model for dust emission by saltation bombardment. *J. Geophys. Res-Atmos.*, 104, 16827-
502 16842, <https://doi.org/10.1029/1999JD900169>, 1999.

503 Marticorena, B., Bergametti, G., Aumont, B., Callot, Y., N'Doume, C. and Legrand, M., Modeling the atmospheric dust
504 cycle: 2. Simulation of Saharan dust sources. *J. Geophys. Res.*, 102D(4), 4387–4404,
505 <https://doi.org/10.1029/96JD02964>, 1997.

506 Martin, R. L. and Kok, J.F., Wind-invariant saltation heights imply linear scaling of aeolian saltation flux with shear stress.
507 *Science Advances*, Vol. 3, no. 6, e1602569, DOI: 10.1126/sciadv.1602569, 2017.

508 Mikami, M., Yamada, Y., Ishizuka M., Ishimaru, T., Gao, W. and Zeng, F., Measurement of saltation process over gobi and
509 sand dunes in the Taklimakan desert, China, with newly developed sand particle counter. *J. Geophys. Res-Atmos.*, 110,
510 D18S02, <https://doi.org/10.1029/2004JD004688>, 2005.

511 Owen, R. P., Saltation of uniform grains in air. *J. Fluid. Mech.*, 20, 225–242, <https://doi.org/10.1017/S0022112064001173>,
512 1964.

513 Pisso, I., Sollum, E., Grythe, H., Kristiansen, N., Cassiani, M., Eckhardt, S., Arnold, D., Morton, D., Thompson, R. L.,
514 Groot Zwaaftink, C. D., Evangelidou, N., Sodemann, H., Haimberger, L., Henne, S., Brunner, D., Burkhart, J. F.,
515 Fouilloux, A., Brioude, J., Philipp, A., Seibert, P., and Stohl, A., The Lagrangian particle dispersion model FLEXPART
516 version 10.4. *Geosci. Model Dev.*, 12, 4955–4997, <https://doi.org/10.5194/gmd-12-4955-2019>, 2019.

517 Raupach, M.R., Drag and drag partition on rough surfaces. *Boundary-Layer Meteorol.*, 60, 375–395.
518 <https://doi.org/10.1007/BF00155203>, 1992. Reid, J. S., Reid, E. A., Walker, A., Piketh, S., Cliff, S., Al Mandoos, A., Tsay,
519 S.-C. and Eck, T. F., Dynamics of southwest Asian dust particle size characteristics with implications for global dust
520 research. *J. Geophys. Res-Atmos.*, 113, D14212, <https://doi.org/10.1029/2007JD009752>, 2008.

521 Rice, M. A., Willetts, B. B. and McEwan, I. K., An experimental study of multiple grain-size ejecta produced by collisions
522 of saltating grains with a flat bed. *Sedimentology*, 42, 695-706. <https://doi.org/10.1111/j.1365-3091.1995.tb00401.x>, 1995.

523 Rice, M. A., Willetts, B. B. and McEwan, I. K., Observations of collisions of saltating grains with a granular bed from high-
524 speed cine-film. *Sedimentology*, 43, 21-31, <https://doi.org/10.1111/j.1365-3091.1996.tb01456.x>, 1996.

525 Rosenberg, P. D., Parker, D. J., Ryder, C. L., Marsham, J. H., Garcia-Carreras, L., Dorsey, J. R., Briiks, I. M., Dean A. R.,
526 Crosier J., McQuaid, J. B. and Washington, R., Quantifying particle size and turbulent scale dependence of dust flux in the
527 Sahara using aircraft measurements, *J. Geophys. Res-Atmos.*, 119, 7577–7598, <https://doi.org/10.1002/2013JD021255>,
528 2014.

529 Shao, Y., A model for mineral dust emission. *J. Geophys. Res-Atmos.*, 106, 20239-20254, [https://doi.org/10.1029/](https://doi.org/10.1029/2001JD900171)
530 2001JD900171, 2001.

531 Shao, Y., Simplification of a dust emission scheme and comparison with data. *J. Geophys. Res.*, 109,
532 <https://doi.org/10.1029/2003JD004372>, 2004.

533 Shao, Y., *Physics and Modelling of Wind Erosion*. Springer, <https://doi.org/10.1007/978-1-4020-8895-7>, 2008.

534 Shao, Y., Ishizuka, M., Mikami, M. and Leys, J. F., Parameterization of size-resolved dust emission and validation with
535 measurements. *J. Geophys. Res.-Atmos.*, 116, D08203, <https://doi.org/10.1029/2010JD014527>, 2011.

536 Shao, Y. and Mikami, M., *Heterogeneous Saltation: Theory, Observation and Comparison*. *Boundary-Layer*
537 *Meteorol.*, 115, 359–379, <https://doi.org/10.1007/s10546-004-7089-2>, 2005.

538 Shao, Y., Raupach, M. R. and Findlater, P. A., Effect of saltation bombardment on the entrainment of dust by wind. *J.*
539 *Geophys. Res.-Atmos.*, 98, 12719-12726, <https://doi.org/10.1029/93JD00396>, 1993.

540 Sow, M., Alfaro, S., Rajot, J. L., Marticorena, B., Size resolved dust emission fluxes measured in Niger during 3 dust storms
541 of the AMMA experiment. *Atmos. Chem. Phys.*, 9, 3881-3891, <https://doi.org/10.5194/acp-9-3881-2009>, 2009.

542 Sterk G., Jacobs A.F.G. and van Boxel J.H., The effect of turbulent flow structures on saltation sand transport in the
543 atmospheric boundary layer. *EARTH SURF. PROC. LAND.*, 23, 877 - 887, [https://doi.org/10.1002/\(SICI\)1096-](https://doi.org/10.1002/(SICI)1096-9837(199810)23:10<877::AID-ESP905>3.0.CO;2-)
544 [9837\(199810\)23:10<877::AID-ESP905>3.0.CO;2-](https://doi.org/10.1002/(SICI)1096-9837(199810)23:10<877::AID-ESP905>3.0.CO;2-), 1998.

545 Stout, J.E., Zobeck, T.M., Intermittent saltation. *Sedimentology*, 44, 959–970, [https://doi.org/10.1046/j.1365-3091.1997.d01-](https://doi.org/10.1046/j.1365-3091.1997.d01-55.x)
546 55.x, 1997.

547 Stull, R. B., *An Introduction to Boundary Layer Meteorology*. Kluwer Academic Publishers, Boston,
548 <http://dx.doi.org/10.1007/978-94-009-3027-8>, 1988.

549 Ungar, J.E. and Haff, P.K., Steady state saltation in air. *Sedimentology*, 34, 289–299, [https://doi.org/10.1111/j.1365-](https://doi.org/10.1111/j.1365-3091.1987.tb00778.x)
550 3091.1987.tb00778.x, 1987.

551 Walklate, P.J., A random-walk model for dispersion of heavy particles in turbulent air flow. *Boundary-Layer*
552 *Meteorol* 39, 175–190, <https://doi.org/10.1007/BF00121873>, 1987.

553 Wang, L., and D. E. Stock, Dispersion of Heavy Particles by Turbulent Motion. *J. Atmos. Sci.*, **50**, 1897–
554 1913, [https://doi.org/10.1175/1520-0469\(1993\)050<1897:DOHPBT>2.0.CO;2](https://doi.org/10.1175/1520-0469(1993)050<1897:DOHPBT>2.0.CO;2), 1993.

555 Webb, N. P., Chappell, A., LeGrand, S. L., Ziegler, N. P., Edwards, B. L., A note on the use of drag partition in aeolian
556 transport models. *Aeolian Research*, 42, <https://doi.org/10.1016/j.aeolia.2019.100560>, 2019.

557 Yahaya, S., Frangi, J. P. and Richard, D. C., Turbulent characteristics of a semiarid atmospheric surface layer from cup
558 anemometers - Effects of soil tillage treatment (Northern Spain). *Annales Geophysicae*, 21: 2119-2131,
559 <https://doi.org/10.5194/angeo-21-2119-2003>, 2003.

560 Zender, C.S., Bian, H., Newman, D., Mineral Dust Entrainment and Deposition (DEAD) model: Description and 1990s dust
561 climatology. *J. Geophys. Res.*, 108: 4416, <https://doi.org/10.1029/2002JD002775>, 2003.

562